Design of a Scratching Damper for Identification of Young's Modulus and Hardness of Extruded Aluminum

Chun Nam Wong , Anand VYAS , Wai On WONG * , Ruqi Sun

Posted Date: 7 May 2024

doi: 10.20944/preprints202405.0386.v1

Keywords: scratching damper; scratch energy conservation; right-angled scratch head; extruded aluminum; Brinell hardness

Article

Design of a Scratching Damper for Identification of Young's Modulus and Hardness of Extruded Aluminum

Chun Num Wong [1], Anand Vyas [2], Wai On Wong [1,*] and Ruqi Sun [3]

[1] Department of Mechanical Engineering, The Hong Kong Polytechnic University, Hongkong, China
[2] Division of Science, Engineering and Health Studies, CPCE, The Hong Kong Polytechnic University, Hongkong, China
[3] School of Automobile, Chang'an University, Xian, China
* Correspondence: wai.on.wong@connect.polyu.hk

Abstract: A special vibration damper is proposed for material property identification through a scratching process on a vibrating object. This paper presents the design and working principle of a scratching damper based on a scratch test device. A non-contact electromagnetic shaker is used to generate the shaking force for the vibration of the tested object. The required pressure on the scratched material during the scratching process is generated by a compression spring and adjusted by changing the amount of compression of the spring. The proposed damper is designed and tested on extruded aluminum samples for the determination of its Young's modulus and hardness and validated by using the standard test instruments. Observations of physical dimensions of the scratching tracks are determined by microscope and were utilized to compute the scratching energy factor. Load curves are obtained at different pressure of the scratching process. The hysteresis loop energy during the scratching process of the tested object is measured and used for the determination of material properties of the object. Furthermore, energy conservation law, scratch energy release rate and loop energy release rate are used to determine the Young's modulus and hardness of the sample. The measurement accuracy of the modulus and hardness of the tested sample is evaluated. The proposed method of material testing has several advantages over the traditional methods such as low cost and high repeatability, and may be used as an alternative to the standard modulus and hardness testers.

Keywords: scratching damper; scratch energy conservation; right-angled scratch head; extruded aluminum; Brinell hardness

1. Introduction

In order to acquire the material property by scratch test, different experimental processes and analytical methods have been implemented. Kamplade and Biermann [1] utilized scratch tests analyzing the grain performance while grinding thermoplastics. Corundum grains were used in two different scratch test set-ups for fundamental analysis of the material removal process. The scratching process was evaluated by the relative material removal volumes of the scratch grooves. In addition to that, the forces occurring during the process and the required specific scratch energy were analyzed. Scratch tests using Rockwell-C diamond cone indenter are reported by Varga et. al. [2] where test load was induced with slip-stick mechanism. Line scars were produced on the specimen after scratching. Scratch topographies and average profiles for increasing scratch load were studied and its cross-section was analyzed. Moreover, study on numerical simulations of the scratch process are also reported using smooth particle hydrodynamics [3].

Through a thorough examination of the failure processes acting at both the macroscopic and microscopic length scales, the fracture toughness was determined using scratch tests. Energy

 doi:10.20944/preprints202405.0386.v1

required to create a unit fracture surface was computed by Akono and Ulm [4] using energetic contour-independent J-integral. Energy release rate was linked to stress intensity factors in mode I and II via the Griffith-Irwin equation [5]. J-integral formulations are reported for micro-scratch test. Finite element meshing was performed on crack tip. Using fracture criterion, forces and the tool geometry were linked to the plane strain fracture toughness [6]. Cross-sectional investigations were done and analyzed. Moreover, it is reported [7] that the elastic modulus and hardness of silicon carbide particle reinforced aluminum matrix composites, SiCp/Al, were determined through the indentation test by loading onto Al matrix and SiC particles, respectively. Two fundamental parameters, the elastic modulus (E) and the hardness (H), can be found by interpreting the *P-h* behavior. Results show that due to the interaction effects of the three phases during the deformation process, when the indenter was on a single phase, the influence of the other phases cannot be neglected and are reflected in the P-h curves. In addition, scratch force, friction coefficient and material removal behaviour were investigated by traditional scratch test and ultrasonic vibration assisted machining (UVAM) tests. In traditional scratch test using single scratch approach, investigations on material removal behavior at the microscale is reported. Referring to the material removal behavior, another report [] states that macroscale grinding process is the compilation of microscopic effects of individual abrasive grains and interactions of neighboring grains were not included. In addition, use of unconventional UVAM technique is basically for difficult-to-process materials. UVAM was a combination of precision or ultra-precision machining with micro-scale (1–15 μm) and high frequency (16–40 kHz) tool or workpiece vibration in one or two directions. In this paper, authors bring test dimension upward to meso-scale of 1mm and lower frequency at 10Hz.

Moreover, mechanism for material removal and crack propagation in glass-ceramic has been studied by scratch test [8]. Increase in the scratch depth leads to the formation of cracks. Material peeling is observed which is due to the crack propagation. Also, material peeling is shown to be obvious in brittle mode whereas plastic ridges are dominant in the ductile mode. Scratch test on glass-ceramics, also show that crack propagation increases linearly with the material removal volume. Wakeel and Hubler [9] introduced heterogeneity into the micro-scratch test fracture. Same formula is utilized in our derivation. In this, the region ahead of the crack tip where material failure occurs is used to determine the energy release rate accounting for heterogeneity of the region. Akono and Ulm [10] established the fracture scaling relations for scratch tests of axisymmetric shape of a scratch indenter in which equivalent force is composed of scratch force and indentation force. In our analysis, the factor for conical indenter is equal to one. Kamplade and Biermann [11] examined the material removal of unreinforced, thermoplastic polymers by scratch tests to analyse the grain engagement. In this, helical scratch groove was produced using single grain. Also, indentation force and specific scratch energy were measured at specific wheel speed.

Material qualities of aluminum alloy have a significant impact on their structural behaviour. Along the line to determine the Young's modulus of aluminum, several aspects considered are ultimate stress, Young's modulus and ultimate strain of normal and high strength aluminum alloys at elevated temperatures [12].

In traditional scratch test, static load is applied to obtain the fracture surface where the test is one time in a direction and is not repeatable. It might be unstable indenter movement along the path, depending on material-indenter interaction. In our case, cyclic vibration load is used instead generating repeatable load-path loop. As a result, stable linearized fracture surface is created. This generates refined sub-layer scratching within test material facilitating in-depth property analysis. Moreover, in the computation of scratch damping ratio, load profile at scratch path, vibrational speed, normal and shear stresses at indenter tip are utilized. Besides, indenter is changeable from round head shaped for slight scratching to pin head shaped in significant scratching.

2. Design and Working Principle of Scratching Damper

An innovative damper is built to conduct divisional scratching test through scratch damping where the required load can be obtained by moving circular scale divisions. Test-rig schematic of the scratching damper is illustrated in Figure 1.

 doi:10.20944/preprints202405.0386.v1

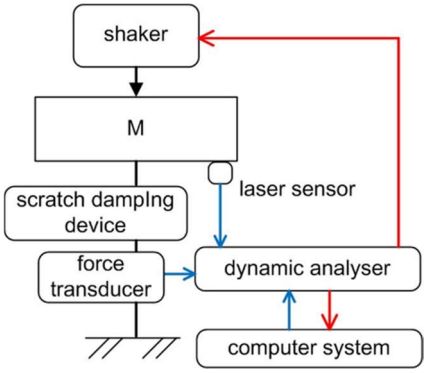

Figure 1. Equipment schematic of scratching damper.

Non-contact electromagnetic exciter is mounted on top of the mounting frame that provides the excitation force without introducing any additional stiffness to the dynamic system as shown in Figure 2. The exciter coil is fixed on the mounting frame while the permanent magnets of the exciter are fixed on the damper system which can be regarded as part of the system mass. Mass, stiffness and natural frequency of damper system are 6.87 Kg, 20.961 N/mm and 9Hz respectively.

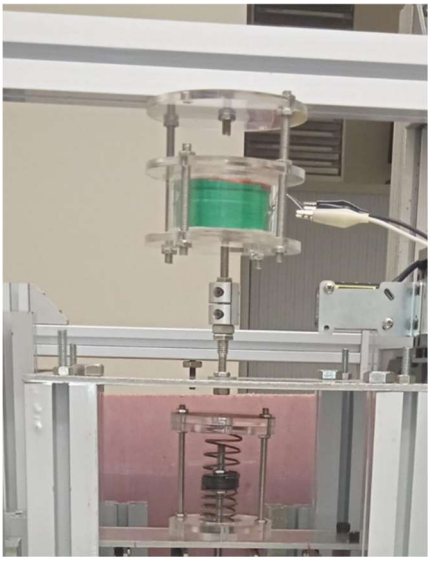

Figure 2. Electromagnetic exciter and its mounting to system mass.

The linear guide is composed of 4 rotation bearings on each side face, and the smooth glassy surface for bearing motion allows reducing the parasitic damping of the damper system. To measure the damper force, force sensor is fastened on the damper rob which is grounded to steel table (Figure 3).

 doi:10.20944/preprints202405.0386.v1

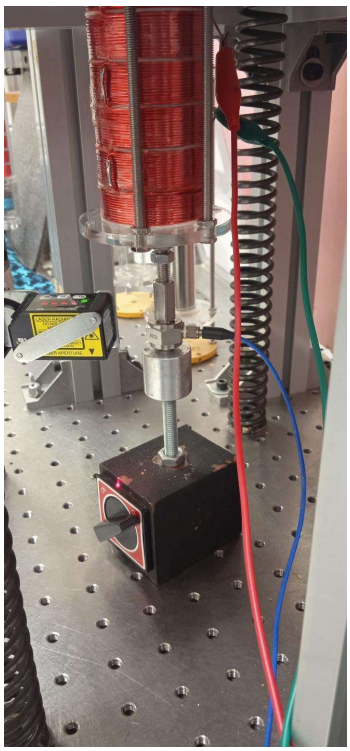

Figure 3. Force transducer assembly of damper rob and magnetic block of scratching damper.

Laser sensor is used to measure the absolute displacement of system mass. A nylon tube, with a pre-compressed spring inside, is fixed on the tuning mechanism of scratching device to provide rough linear guide for the mass vibration. The data acquisition and signal generation are conducted with the B&K PULSE 7767 system (Figure 1). The driving signal to the exciter is amplified by the B&K 2712 power amplifier before sending to the non-contact exciter. The device is installed in the middle part of the system (Figure 4).

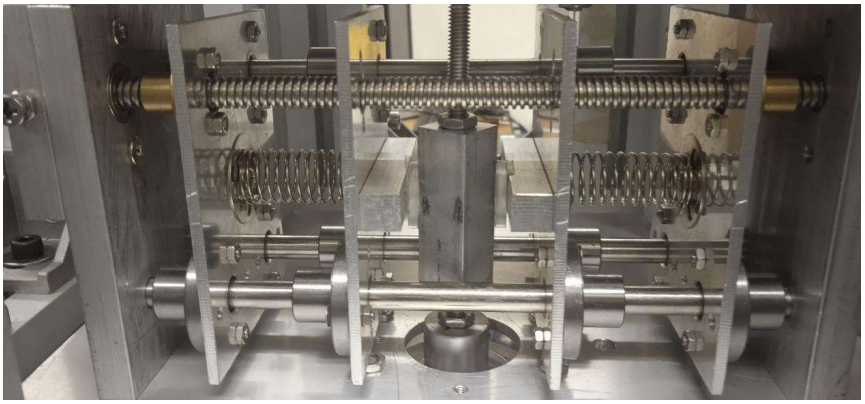

Figure 4. Assembly components of scratching device in scratching damper.

Under the principle of scratch energy conservation, divisional scratching energy is computed by the energy equation within the same interval test

$$U^{ji} = \wp_j^i + \Psi^{ji} \qquad (1)$$

where U^{ji} is j divisional total energy of scratching motion at i^{th} interval, Ψ^{ji} is j divisional energy of damping motion, $\wp_j^i = F_\upsilon^{ji} \cdot \upsilon_j^i$ is j divisional scratching energy, F_υ^{ji} is j divisional scratching energy factor, υ_j^i is j divisional material removal volume.

 doi:10.20944/preprints202405.0386.v1

Applying the energetic contour-independent *J*-integral [4], the scratch energy release rate, which being the energy required to create a unit scratching surface, is

$$\wp = \frac{1}{p}\int_S \left(\Psi n_x - \tau_x \frac{\partial U_x}{\partial x} \right) dS \qquad (2)$$

where $\Psi = \frac{\kappa}{2E}\sigma_{xx}^2$ is free energy density with $\kappa = 1-\nu^2$, ν being Poisson's ratio, $\frac{\partial U_x}{\partial x}$ is displacement gradient, $\tau_x = \sigma_{xx} n_x$ is surface traction. For tangential track generating from the scratch head, Airy stress function is established as

$$\Gamma(x,z) = -ax\left(z^3 - \frac{3}{4} z d^2 \right) + bz^2 \qquad (3)$$

Its symmetric stress tensors are computed by

$$\sigma_{xx} = \frac{\partial^2 \Gamma}{\partial z^2} = -6axz + b \qquad (4)$$

$$\sigma_{xy} = \frac{\partial^2 \Gamma}{\partial x \partial z} = a\left(3z^2 - \frac{3}{4} d^2 \right) \qquad (5)$$

$$\sigma_{zz} = \frac{\partial^2 \Gamma}{\partial x^2} = 0 \qquad (6)$$

Displacement gradient at the scratch head-material interface is determined by the potential function

$$\Theta = -\frac{a}{2}\left[-\frac{x^4 + z^4}{2} + 3(xz)^2 \right] + 2bxz \qquad (7)$$

which satisfying $\Theta_{,zz} = 0$, $\Theta_{,xz} = \sigma_{xx}$. Afterwards, displacement gradient is calculated by

$$\frac{\partial U_x}{\partial x} = \frac{1}{E}\left[-(1+\upsilon)\frac{\partial^2 \Gamma}{\partial x^2} + \kappa \frac{\partial^2 \Theta}{\partial z \partial x} \right] = -6axz + b = \frac{\kappa}{E}\sigma_{xx} \qquad (8)$$

Substituting this to Eq.(2), one can obtain

$$\wp = \frac{1}{p}\int_S -\frac{\kappa}{2E}\sigma_{xx}^2 n_x dS = \frac{\kappa}{2pE}\int_A \sigma_{xx}^2 dA' \qquad (9)$$

On the other hand, the tangential force is given by

$$F_t = \int_S \sigma_{xx} n_x dS = \int_A \sigma_{xx} dA' \qquad (10)$$

Assume that stress field over the scratch head being constant, its linear stress average is related to quadratic stress average on the projected contact area as the integral in Eq. (9) is

$$\int_A \sigma_{xx}^2 dA' \simeq \left(\int_A \sigma_{xx} dA' \right)^2 \Big/ \int_A dA' = \frac{F_t^2}{A} \qquad (11)$$

Preprints.org (www.preprints.org) | NOT PEER-REVIEWED | Posted: 7 May 2024 doi:10.20944/preprints202405.0386.v1

As $F_t \gg F_n$, the equivalent force can be simplified to $F_{eq} = F_t$. Hence we have the scratch energy release rate created as

$$\wp = \frac{1-\nu^2}{E}\frac{F_{eq}^2}{2pA} \tag{12}$$

where E is Young's modulus, p and A are scratch head perimeter and projected contact area respectively. In general, the right -angled scratch head shape function defined by Figure 5 can be generated by

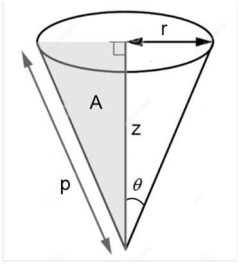

Figure 5. Dimensions of scratch pin head.

$$z = r\cot\theta \tag{13}$$

in which r is radius of head, z is height, θ is conical angle. Firstly, p projected onto scratch direction is

$$p = \int ds = \int_0^{d/B} \sqrt{1+\cot\theta^2}\, dr = \frac{d}{\cot\theta}\sqrt{1+\cot\theta^2} = \frac{d}{\cos\theta} \tag{14}$$

Secondly, scratch surface projected in the scratch direction becomes

$$A = \int n_x dS = \int \hat{n}\cdot e_x r\sqrt{1+\cot\theta^2}\, d\phi dr \tag{15}$$

where $\hat{n} = \frac{\cot\theta\cos\phi}{\sqrt{1+\cot\theta^2}}e_r + \frac{1}{\sqrt{1+\cot\theta^2}}e_z$. Therefore A can be computed using cylindrical co-ordinate as

$$A = \int_0^{d/B}\int_0^{\pi/2} \cot\theta\left(\cos\phi r\right) d\phi dr = \frac{\cot\theta}{2}\left[\sin\phi\big|_0^{\pi/2}\right]\left[r^2\big|_0^{d/B}\right] = \frac{d^2\tan\theta}{2} \tag{16}$$

3. Results and Discussions

3.1. Young's Modulus of Extruded Aluminum Flat Bar

Upon scratch test of an extruded aluminum flat bar sample as shown in Figure 6 of size 15(L)x10(W)x4(T) in mm using scratching damper, the following sample tests in two to four divisions of the compression of spring pressure are conducted to investigate its material properties (such as Young's modulus, hardness) in Figure 7.

 doi:10.20944/preprints202405.0386.v1

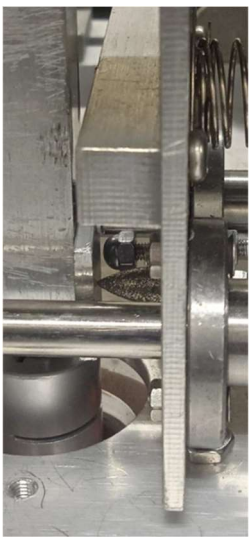

Figure 6. Scratching test of extruded aluminum using pin and round heads.

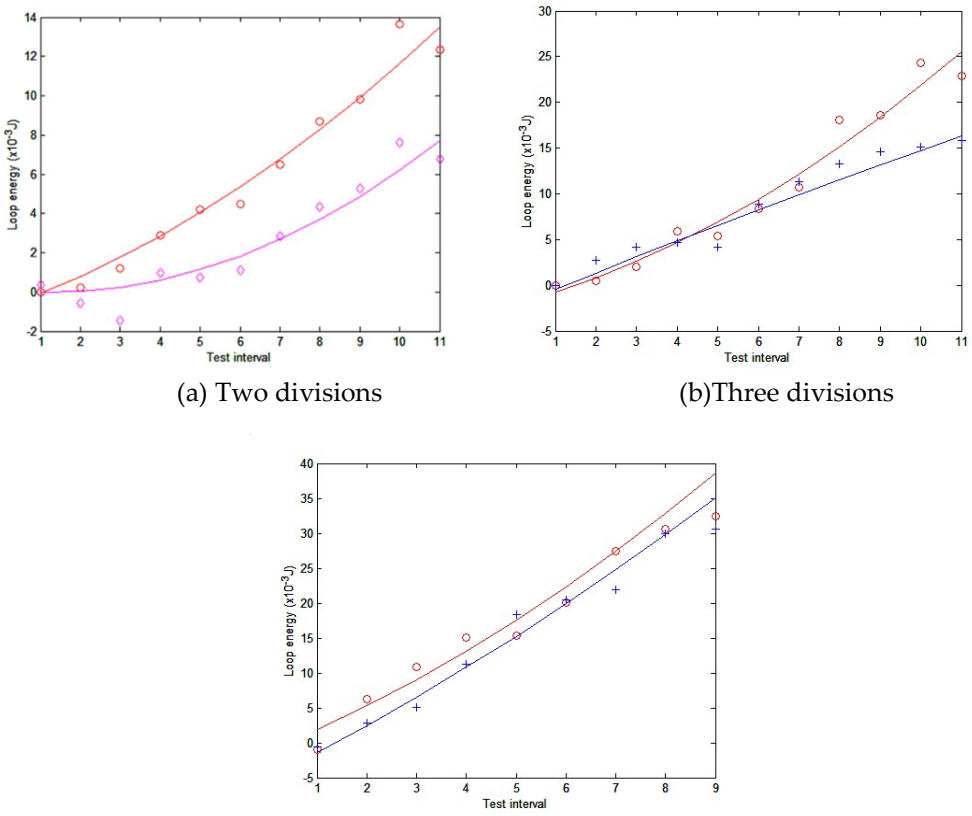

(a) Two divisions (b)Three divisions

(c) Four divisions

Figure 7. Divisional loop energy curves of extruded aluminum.

These load curves indicate that loop energy increases linearly with the interval load [5–8]. Some of the results are complied with Akono and Ulm [7–10] that scratching energy release rate increases with test load in quadratic curve. From Table 1, one observes that normal force increases linearly with two to four dial divisions. However, the profile of loop damping energy per interval remains relatively constant.

 doi:10.20944/preprints202405.0386.v1

Table 1. Extruded aluminum material property comparison from scratching test.

Data \ Dial division	2	3	4
Normal force (N)	0.16	0.24	0.32
Total energy (J)	35.2	56.5	78.8
Damping motion energy(J)	24.8	47.8	70.3
Scratch energy (J)	10.4	8.69	8.51
Scratch performance (%)	29.5	15.4	10.8
Young's modulus (GPa)	54.6	56.2	56.8
Hardness (GPa)	76.8	78.0	80.5
Scratch depth(mm)	0.193	0.176	0.180
Scratch length(mm)	3.38	3.10	2.92
Scratch volume(mm^3)	0.183	0.160	0.141
Fv(GJ/m^3)	56.8	54.5	60.2

The summation of loop energy per interval with pin conical rod is divisionals' total energy expressed as

$$U_{pin}^{j}=\sum_{i=1}^{N}U_{pin}^{ji}\cdot j\cdot f_t\cdot l_t/2=U_t^j \tag{17}$$

where U_{pin}^{ji} is single loop energy with pin rod, i is number of test interval, j is dial division of the test, f_t=9 Hz is fixed-sine test frequency, l_t = 48s is the test period. It is interesting to observe that shape of loop is highly repeatable within the same test period with nearly 500 cycles. Meanwhile, the summation of loop damping energy per interval with round rod is expressed as

$$\Psi_{round}^{j}=\sum_{i=1}^{N}\Psi_{round}^{ji}\cdot j\cdot f_t\cdot l_t/2=\Psi_j \tag{18}$$

where U_{round}^{ji} is single loop energy with round rod. By Eq.(1), scratching energy per interval with j divisions is

$$\wp_j=U_{pin}^{j}-\Psi_{round}^{j} \tag{19}$$

Divisional scratching energy release rate is

$$\wp_j=\sum_{i=1}^{i=N}\frac{\wp_j^i}{N\cdot j} \tag{20}$$

Meanwhile by Eq. (12), divisional Young's modulus stands as

$$E_j=\frac{1-\nu^2}{\wp_j}\times\frac{Feq_j^2}{2p_jA_j} \tag{21}$$

with notations in j divisions. Results from two to four divisions are input to Table 1. In general, their values decrease slightly with scratch performances and they tend to underestimate the actual E. High performance indicates that scratching process follows scratch energy release rate. Two divisions is the best at 29.5%. Thus, by two divisional test, its ith interval E_2^i is generated. From its Nth data, ultimate Young's modulus is obtained as $E_2^N=54.6\times10^9 GPa$.

Tensile test is utilized to validate the Young's modulus of extruded aluminum. Sample of nominal size in mm 57.4(L)x19.1(W)x2.76(T) is prepared conforming to the ASTM E 21 standards. Tensile testing machine is set to pull the sample as shown in Figure 8 until its fracture is exhibited (Figure 9). Stress and strain are calculated during the test by recording the applied tensile load and extension.

 doi:10.20944/preprints202405.0386.v1

Figure 8. Tensile test of extruded aluminum sample.

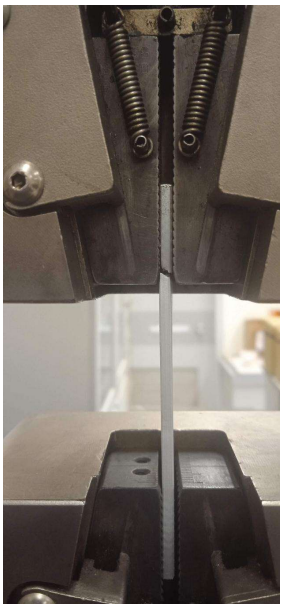

Figure 9. Fracture of extruded aluminum sample during tensile test.

Stress-strain curve is generated by the machine as shown in Figure 10.

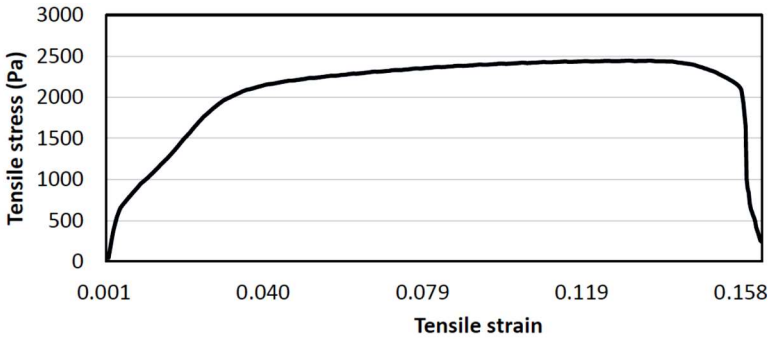

Figure 10. Stress-strain curve generated by tensile testing machine.

According to the analysis of Su and Young [9–12], Young's modulus of extruded aluminum varies linearly in initial stage of this curve. In the linear elastic region, the material behaves elastically, and the value of the Young's modulus remains relatively constant. It is important to note that that as

 doi:10.20944/preprints202405.0386.v1

the material gets closer to its yield point, the point at which plastic deformation starts, this linear connection could not hold true at greater stress levels. Young's modulus will go down as the substance experiences plastic deformation. By examining the change in stress and strain values at distinct positions within the linear section, insights into the material's behaviour can be sought and Young's modulus based on the ratio of the changes in stress and strain can be calculated. In our case, change in stress and strain at separate positions 1 and 2 of linear section are computed. Slope of the curve is used to calculate the Young's modulus of this sample as

$$E^T = \frac{\Delta\sigma}{\Delta\delta} = \frac{\sigma_2^T - \sigma_1^T}{\delta_2^T - \delta_1^T} \times \frac{L}{WT} \tag{22}$$

The generated value is $E^T = 57.2GPa$ which is +4.55% larger than E_2^N. Positive deviation arises at the elastic region estimation by tensile test. Thus, it tends to overestimate E_2^i at plastic region. For extruded aluminum, it's normalised dependence of Young's modulus ratio $E_r = E_a / E_o$ on the apparent density $\rho_r = \rho_a / \rho_o$ for flat bar sample [11–14] is

$$E_r = w\rho_r^u \tag{23}$$

where w = 0.974 is fitting constant, u is fitting exponent. Using digital weight test, experimental ρ_r is found to be 0.91. Substituting ρ_r and $E^T = 57.2GPa$ into this equation, u is determined to be 1.479. Now substituting the scratch $E_r = 0.578$ into Eq. (23), scratch ρ_r is computed as 0.844 which being -7.2% deviation from experimental value.

3.2. Hardness Estimation and Brinell Test

Hardness of extruded aluminum is computed as follows. Divisional contact stiffness is given as

$$\frac{dP_j^i}{dH_j^i} = \frac{\beta}{\sqrt{\pi}} \times \frac{Feq_j^{i\,2}}{p_j^i \wp_j^i \sqrt{A_j^i}} \tag{24}$$

where β is the scratch head correction factor. From this equation, hardness is computed. Its four divisions *P-h* curve is best fitted with results of Zheng et al. [7]. Thus, it is used for analysis of divisional hardness. Meanwhile, divisional hardness is computed as

$$H_j^i = \frac{P_j^i}{A_j^i} \tag{25}$$

Using load data from two to four divisions, their hardness are generated in Table 1. They increase with the divisional number. Using four divisional test, ultimate hardness is calculated using its *N*th data as

$$H_4^N = \frac{P_4^N}{A_4^N} = 80.5GPa \tag{26}$$

For existing standard tests, hardness can be measured through hardness tester and tensile test. Considering the Brinell hardness tester in Figure 11 illustrating principle of the Brinell indenting process, an indenting load of 100 *Kgf* is exerted on the surface of the extruded aluminum sample plate through hardened steel ball of 1/16 inch diameter. After applying the load, a holding time of 15 s was used to ensure that the plastic flow of the testing material has ceased. It can avoid indenter from springback action and prevents from obtaining inaccurate diameter of the indented impression. The Brinell hardness number is related to the average flow stress of the material in the volume subjected to plastic deformation. Also, the required specifications on sample thickness were followed. The thickness of the specimen was at least ten times the depth of the indentation to avoid any breakage of the sample under high force. It also prevents samples from bending leading to accuracy of the test.

 doi:10.20944/preprints202405.0386.v1

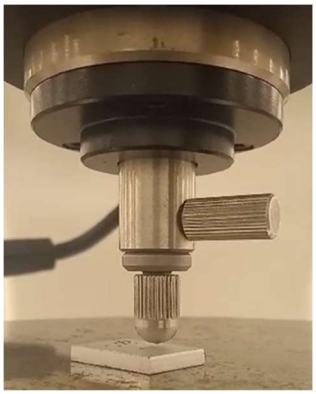

Figure 11. Hardness testing of extruded aluminum sample using steel ball indenter.

Multiple tests were carried out using same size samples. Brinell hardness number was used to compare the actual hardness. The microscopic image of an indentation on an aluminum sample in the specific experiment is shown in Figure 12. Diameter of resulting permanent impression on the sample measured is $594.12\mu m$. Ultimately, Brinell hardness number [12–15] is computed as

$$B_h = 2P_b \Big/ \left(\pi D_s \left(D_s - \sqrt{D_s^2 - d_I^2} \right) \right) = 75.0 \tag{27}$$

where $P_b = 100kgf$ is the load on the indenting tool, $D_s = 1.59mm$ is the diameter of steel ball, $d_I = 1.19mm$ is measured diameter at the rim of indentation. As compared with H_4^N, percentage difference is -6.89%. Negative deviation arises at estimation of higher peak load by the damper near the plastic region. Thus, it tends to overestimate B_h at elastic region. Material with lower modulus of elasticity will have a lower BHN. The modulus of elasticity of a material is the cause for the BHN of that material. The materials' modulus of elasticity here indicates how resistant it is to elastic deformation when stress is applied to it. The modulus of elasticity has affected the hardness of the material. Note that BHN has the dimension of stress but is usually quoted by mass per unit area.

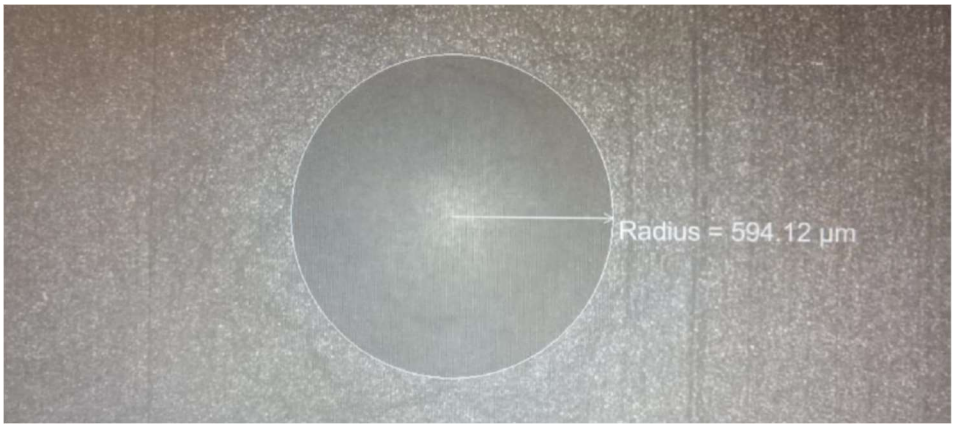

Figure 12. Steel ball indentation on extruded aluminum sample.

Additionally, using the stress-strain curve of tensile test at 0.2% plastic deformation, the offset yield strength is taken as 72.1*GPa*. By the interpolated data curve, this corresponds to tensile test hardness H^T of 77.7*GPa*. Comparing with the H_4^N, it is only -3.15% deviated. Hence scratch hardness computed by Eq.(25) is fully validated.

3.3. Dimension Inspection and Performance Evaluation

In order to check the physical depth of the scratching track, laser sensor (Figure 13) is used to measure the depth of each track on the divisional samples (Figure 14).

 doi:10.20944/preprints202405.0386.v1

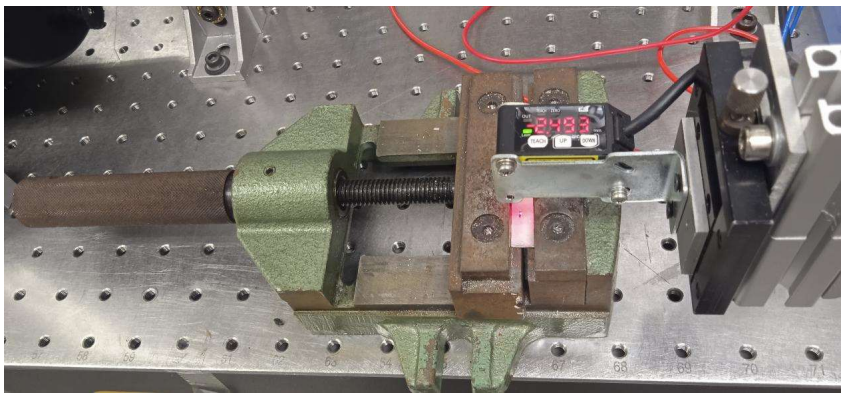

Figure 13. Experimental set-up of laser depth test.

Figure 14. Extruded aluminum sample used in laser depth test.

Moreover, microscope shown in Figure 15 is used to determine the physical dimensions of the scratching track (Figure 16) which were smooth and measurable.

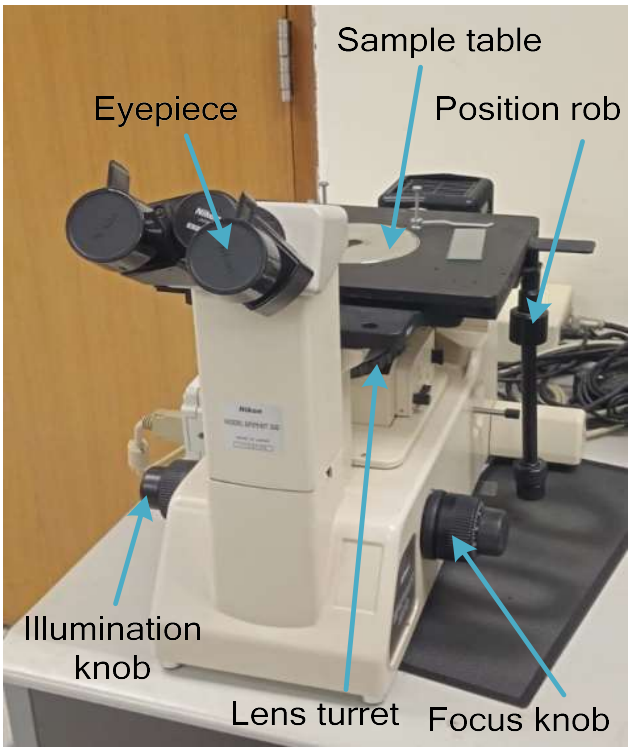

Figure 15. Microscope inspection of extruded aluminum sample.

 doi:10.20944/preprints202405.0386.v1

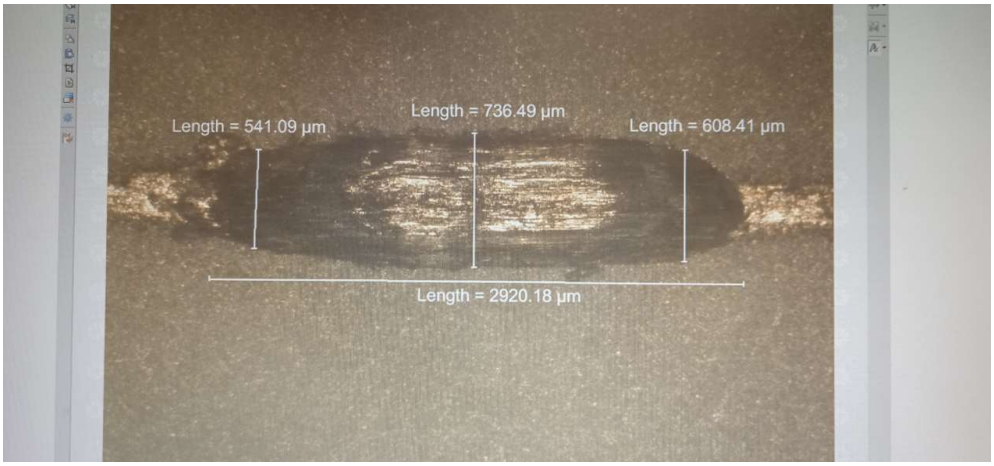

Figure 16. Scratching track of extruded aluminum sample.

The data measured from the scratch test is shown in Table 1 and was used to compute the material removal volume υ. The scratching energy factor at *j* division, F_{υ} is computed by Eq.(1) as listed in Table 1. From Table 1, it is observed that U^j increases linearly with *j*. Simultaneously, Ψ^j increases with *j* with larger linear rate. As a result, $\wp_j$ decreases with *j* but gets saturated at four divisions test. Overall scratching performance $\wp_j / U^j$, decreases with *j*. This is in agreement with the slightly increasing trend seen in E_j and H_j estimations. On the other hand, F_{υ}^j is fluctuating around a constant value and is independent of the performance. Hence it is independent of *i* or *j*, and is in agreement with the energy conservation principle in Eq. (1).

4. Conclusions

In this paper, a scratching damper is developed based on the scratching device. Cyclic vibration load is applied by the damper creating highly repeatable load-path loop. Smooth fracture surface was obtained and was measurable at microscopic scale. Round head indenter is used to provide pure damping motion, while pin head indenter is used to produce significant scratching motion. Scratching energy release rate was generated using free energy density and displacement gradient. Ψ^{ji} and U^{ji} are computed to estimate $\wp_j^i$. F_{υ}^j is found to be stable round $56.8GJ/m^3$ agreeing with the energy conservation principle. Upon comparing the Young's modulus, E^T from tensile test, it is 4.55% more than that of E_2^i obtained from scratch test. Moreover, hardness, H_4^N is only 6.89% more than B_h. The results discussed here furthers work into innovative methods in developing devices and approaches to determine material properties.

Author Contributions: Conceptualization, CN Wong and WO Wong; methodology, CN Wong and A Vyas.; software, CN Wong.; validation, CN Wong, WO Wong and A Vyas; formal analysis, CN Wong; investigation, CN Wong.; resources, WO Wong and R Sun.; data curation, CN Wong and A Vyas; writing—original draft preparation, CN Wong.; writing—review and editing, A Vyas and WO Wong; visualization, CN Wong and A Vyas ; supervision, WO Wong.; project administration, WO Wong; All authors have read and agreed to the published version of the manuscript.

Funding: This research received no external funding.

Data Availability Statement: Research data may be shared upon request.

Acknowledgments: The authors would like to thank The Hong Kong Polytechnic University for the laboratory support of the experiments in this research.

Conflicts of Interest: The authors declare no conflicts of interest.

 doi:10.20944/preprints202405.0386.v1

References

1. K. Kamplade, D. Biermann, Examination of the Material Removal of unreinforced, thermoplastic Polymers by Scratch Tests, Production Engineering, 13:713-719, 2019
2. M. Varga, S. Leroch, H. Rojacz, M. R. Ripoll, Study of wear mechanisms at high temperature scratch testing, Wear, 388-389, 112-118, 2017.
3. H. Li, X. Zhang, Xiufeng Yang, Numerical study of liquid sloshing using smoothed particle hydrodynamics with adaptive spatial resolution, Engineering Analysis with Boundary Elements, 159, 272-287, 2024
4. A. Akono, F. Ulm, An improved technique for characterizing the fracture toughness crack growth, Wear 313, 117–124, 2014
5. A.R. Torabi, B. Shahbazian, Notch tip plastic zone determination by extending Irwin's model, Theoretical and Applied Fracture Mechanics, 108, 102643, 2020
6. J.M. Souza, H.N. Yoshimura, F.M. Peres, C.G. Schön, Effect of sample pre-cracking method and notch geometry in plane strain fracture toughness tests as applied to a PMMA resin, Polymer Testing, 31(6), 834-840, 2012
7. W. Zheng, Y. Wang, M. Zhou, et.al., Material deformation and removal mechanism of SiCp/Al composites in ultrasonic vibration assisted scratch test, Ceramics International 44, 15133-15144, 2018
8. Z. Qiu, C. Liu, X. Yang, et.al., Crack propagation and the material removal mechanism of glass–ceramics by the scratch test, Mechnical behavior of biomedical materials, 64, 75-85, 2016
9. S. Al Wakeel, M.H. Hubler, Introducing heterogeneity into the micro-scratch test fracture toughness relation for brittle particle composites, Experimental Mechanics, 58, 1237-1247, 2018
10. A. Akono, F. Ulm, Fracture scaling relations for scratch tests of axisymmetric shape, Mechanics and Physics of Solids, 60, 379-390, 2012
11. K. Kamplade, D. Biermann, Examination of the material removal of unreinforced, thermoplastic polymers by scratch tests, production engineering, 13, 713-719, 2019
12. M. Su, B. Young, Material properties of normal and high strength aluminum alloys at elevated temperatures, Thin-Walled Structures, 137, 463-471, 2019
13. L. Hemmouche, D. Chicot, A. Amrouche, et al., An analysis of the elastic properties of a porous aluminum oxide film by means of indentation techniques. Materials Science and Engineering: A, 585, 155-164, 2013
14. J. Kovacik, F. Simancik, Aluminum foam - Modulus of elasticity and electrical conductivity according to percolation theory, Scripta Materialia, 39, 2(239–246), 1998
15. M.M. Ali, A.N.M. Omran, M.A. Mohamed, Prediction the correlations between hardness and tensile properties of aluminum-silicon alloys produced by various modifiers and grain refineries using regression analysis and an artificial neural network model, Engineering Science and Technology, 24, 105-111, 2021